



Spectral study of faint radio sources in ELAIS N1 field

AKRITI SINHA*, SARVESH MANGLA and ABHIRUP DATTA

Indian Institute of Technology Indore, Indore, India.

*Corresponding author. E-mail: sinha.akriti44@gmail.com

MS received 26 May 2023; accepted 7 August 2023

Abstract. Understanding the spectral properties of sources is crucial for the characterization of the radio source population. In this work, we have extensively studied the ELAIS N1 field using various low-frequency radio observations. For the first time, we presented the 1250 MHz observations of the field using the upgraded Giant Meterwave Radio Telescope (uGMRT) that reach a central off-source RMS noise of $\sim 12 \mu\text{Jy beam}^{-1}$. A source catalog of 1086 sources is compiled at 5σ threshold ($>60 \mu\text{Jy}$) to derive the normalized differential source counts at this frequency, which is consistent with existing observations and simulations. We presented the spectral indices derived in two ways: two-point spectral indices and by fitting a power-law. The latter yielded a median $\alpha = -0.57 \pm 0.14$, and we identified nine ultra-steep spectrum sources using these spectral indices. Further, using a radio color diagram, we identified the three mega-hertz peaked spectrum (MPS) sources, while three other MPS sources are identified from the visual inspection of the spectra, the properties of which are discussed. In our study of the classified sources in the ELAIS N1 field, we presented the relationship between α and z . We found no evidence of an inverse correlation between these two quantities and suggested that the nature of the radio spectrum remains independent of the large-scale properties of the galaxies that vary with redshifts.

Keywords. Radio continuum—galaxies—galaxies—active.

1. Introduction

Investigation of deep radio sky is crucial to examine the population of galaxies at different redshifts. This population is primarily composed of various sources, including star-forming galaxies (SFGs) and active galactic nuclei (AGN). Many galaxies are believed to have supermassive black holes at their centers, which power AGN. The relativistic jets from these AGN also provide feedback, which shapes and affects the galaxy and the intergalactic medium. Therefore, we must comprehend AGN evolution to fully understand galaxies and their evolution (Fabian 2012). Actually, the early evolutionary stages of a radio AGN are still debated (Orienti 2016; Bicknell *et al.* 2018). Due to the similarities between them at the kpc and pc scales, compact radio doubles discovered using Very Long Baseline Interferometry (VLBI), have been proposed as the ancestors of Fanaroff–Riley (FR) types I and II radio-loud AGN (RL AGN; O’Dea & Baum 1997).

The differential source counts are utilized to investigate the nature of extra-galactic sources and galaxy

evolution (Padovani *et al.* 2011, 2015; Prandoni *et al.* 2018). It is observed that the deep radio sky is dominated by RL AGN population at high flux density regimes, whereas the population of SFGs becomes more dominant at lower flux density ends (see, for e.g., Smolčić *et al.* 2008, 2017; Padovani 2016; Best *et al.* 2023), as is reflected from the flattening of the normalized source counts. It also has been found that the fainter flux density regimes also comprise another source population called radio-quiet AGN (RQ AGN) (Padovani *et al.* 2009; Bonzini *et al.* 2013), whose radio emission mechanism is still debated. Some studies like Miller *et al.* (1993) suggested that these sources are mini-scaled versions of RL AGN, while Sopp & Alexander (1991) proposed the radio emissions from these sources are from the star-forming regions of the host galaxies. The recent study by Panessa *et al.* (2019) discussed a wide range of mechanisms responsible for radio emission in the RQ AGN population: AGN-driven wind, star-formation, jets with low power, coronal activity in the innermost accretion disk and free–free emission from the photoionized gas (see Panessa *et al.* 2019, and references therein).

The low-frequency observations are essential for the detection of faint radio sources, also ultra-steep spectrum (USS) sources, which are generally the radio galaxies at high- z (Best *et al.* 2003; Miley & De Breuck 2008). Complementary radio observations at low- and high-frequencies are crucial for the characterization of sources depending on their spectra (Coppejans *et al.* 2015; Mahony *et al.* 2016a). This may lead to the identification of diverse source populations with different spectral properties, e.g., USS sources (Roettgering *et al.* 1994), gigahertz-peaked spectrum sources (GPS) (O’Dea 1998; Athreya & Kapahi 1999) and core-dominated RQ AGN (Blundell & Kuncic 2007).

Furthermore, a family of radio AGN called GPS, compact steep spectrum (CSS) and high-frequency peaked (HFP) sources have been proposed as the young counterparts of enormous RL AGN (Hardcastle *et al.* 2019). HFP sources have spectral peaks above 5 GHz with pc-scale linear sizes, GPS sources peak around 1 GHz with linear sizes ≤ 1 kpc, while CSS sources peak at low frequencies (≤ 500 MHz) and have linear sizes of ~ 1 –20 kpc. Besides these classes of sources, there are recent studies that have found megahertz-peaked spectrum (MPS) sources with a similar spectrum that peak at frequencies below 1 GHz (Coppejans *et al.* 2015; Callingham *et al.* 2017). As a result of cosmic evolution, MPS sources are considered as the amalgamation of nearby CSS sources, and GPS and HFP sources at high redshift whose turnover frequencies have been redshifted to lower frequencies below 1 GHz (Coppejans *et al.* 2016).

There are two debated scenarios for these sources: ‘Youth’ hypotheses, where these sources represent the young precursors of RL AGN (Wilkinson *et al.* 1994; O’Dea 1998; Murgia *et al.* 1999; Orienti *et al.* 2006; An & Baan 2012) or the ‘frustration’ model, where the compact sizes are caused by a dense medium surrounding the nucleus (van Breugel *et al.* 1984; Bicknell *et al.* 1997). By determining whether synchrotron self-absorption (SSA) or free-free absorption (FFA) is in charge of the change in the radio spectrum, one can determine whether a GPS, CSS or HFP source is young or frustrated. A source will typically have optical thickening at low frequencies due to SSA, which is caused by the relativistic electrons themselves and has a characteristic spectral index limit of 2.5 ($S \propto \nu^\alpha$) below the spectral turnover. Moreover, it has been found that FFA presumably dominates the source’s spectrum below the turnover within small spatial scales surrounded by the dense circum-nuclear medium. Most recently, Keim *et al.* (2019) have studied six sources selected from

Callingham *et al.* (2017) in the Galactic and Extragalactic All-sky Murchison Widefield Array survey and suggest FFA as to be the plausible absorption mechanism for their sources.

In this paper, we analysed the uGMRT data at 190 MHz and 1.2 GHz of the ELAIS N1 field to derive the spectral indices of the sources in the 400 MHz radio catalog (see Chakraborty *et al.* 2019) by performing the spectral energy distribution (SED) fitting. Furthermore, for the first time, we identified the MPS sources in the field using a radio color diagram and spectrum. We presented some of their properties here. Using the measured spectral indices from the SED fitting, we also identify USS sources in the field and discussed the variation of α as a function of z for the sources in the field.

2. Observations and analysis

This section is focused on the radio observations carried out in the ELAIS N1 field, which have been utilized in our study. We have utilized the uGMRT data at 400 MHz from Chakraborty *et al.* (2019) and Sinha *et al.* (2022) and extended the analysis, investigating the spectral properties of the faint radio sources in the field. Here, we presented the 1250 MHz uGMRT observations of the ELAIS N1 field followed by a discussion on the other radio continuum data that have been used.

2.1 uGMRT L-band data

For this study, we used archival observations of the ELAIS N1 field ($\alpha_{2000} = 16^{\text{h}}10^{\text{m}}00^{\text{s}}$, $\delta_{2000} = 54^{\text{d}}36^{\text{m}}00^{\text{s}}$) using uGMRT during GTAC cycle 31 (project code: 31_072). These observations are taken for three sessions and the total time for observation (for seven pointings) was 20 h (including calibrators), which centered around 1250 MHz with a total bandwidth of 400 MHz. The ELAIS N1 field was observed during the night time for all the three days on 26 February and 27–28 March 2017. Either 3C 286 or 3C 48 or both are observed at the beginning and at the end for each observing day. The phase calibrator 1634 + 627 near the target field is observed for 5 min between 3 and 4 pointings of the ELAIS N1 field. The total on-source time for every pointing is nearly 130 min. We summarize the observation details in Table 1. In the following sub-sections, we described the data reduction and imaging procedure for creating a mosaic image of the ELAIS N1 field.

Table 1. Observation summary of the calibrator sources and target field (ELAIS N1) for three observing sessions.

Project code	31_072
Observation date	26 February 2017, 27 and 28 March 2017
Bandwidth	400 MHz
Frequency range	1.05–1.45 GHz
Channels	2048
Integration time	16.1 s
Correlations	RR RL LR LL
Flux calibrator	3C 286 and 3C 48
Phase calibrator	1634 + 627
Total on-source time	~15 h (ELAIS N1)
Pointing centers	13 ^h 31 ^m 08 ^s + 30 ^d 30 ^m 33 ^s (3C 286) 16 ^h 34 ^m 34 ^s + 62 ^d 45 ^m 36 ^s (J1634+627) 16 ^h 10 ^m 00 ^s + 54 ^d 40 ^m 00 ^s (target) 16 ^h 10 ^m 00 ^s + 54 ^d 22 ^m 00 ^s (target) 16 ^h 08 ^m 13 ^s + 54 ^d 31 ^m 00 ^s (target) 16 ^h 11 ^m 47 ^s + 54 ^d 31 ^m 00 ^s (target) 16 ^h 08 ^m 12 ^s + 54 ^d 48 ^m 50 ^s (target) 16 ^h 11 ^m 48 ^s + 54 ^d 48 ^m 50 ^s (target) 16 ^h 10 ^m 00 ^s + 54 ^d 57 ^m 50 ^s (target) 01 ^h 37 ^m 41 ^s + 33 ^d 09 ^m 35 ^s (3C 48)

2.2 Data reduction

For the pre-processing of the data, like flagging, radio frequency interference mitigation and calibration, we used ACAL,¹ which is a CASA²-based pipeline. This pipeline only performs direction-independent (DI) calibration solutions and at 1.25 GHz, ionosphere does not corrupt solutions that much, even at low latitude. Each data went through the pipeline for calibration and finally, all the calibrated data of each pointing (Table 1) is used to get the complete image. A brief overview of the pipeline procedure is explained in Sinha & Datta (2023). Now, we splitted the calibrated data of all seven target pointings individually for imaging and self-calibration.

2.3 Imaging and self-calibration

Calibrated data for all the seven pointings is used for imaging individually using WSCLEAN (Offringa *et al.* 2014). Multi-scale wide-bandwidth deconvolution, as described by Offringa & Smirnov (2017) is used to

¹https://github.com/Arnab-half-blood-prince/uGMRT_Calibration_pipeline.

²Common Astronomy Software Applications (<https://casa.nrao.edu/>).

capture the variation in sky brightness across spatial scales. In this study, we chose Briggs robust parameter value of -1 , which ensures uniform weighing across the data. This choice produces a central Gaussian point spread function (PSF), which minimizes the presence of broad wings. To incorporate any bright sources that are located outside the field of view, we generated a large sky map with a size of $\sim 1.1 \text{ deg}^2$ with each pixel with the size of $0.5''$. To optimize the image quality, we performed an initial round of imaging, using the auto-masking algorithm of WSCLEAN with 50 k iterations, down to a significance level of 7σ . Multi-Frequency Synthesis (MFS) image is employed to generate a mask for a subsequent round of imaging. This is a standard procedure to fill the MODEL_DATA column, which is necessary for self-calibration because a model column will be less susceptible to imaging artefacts, resulting in better solutions for subsequent self-calibration loops.

By utilizing the above-explained method, we performed four rounds of phase-only self-calibration procedure with solution intervals (solint) as 8, 6, 4 and 2 min. After incorporating the latest self-calibration solutions, the final image of the target field is generated. However, we did not perform amplitude-only or amplitude-phase self-calibration any further.

After performing self-calibration and separate imaging for each pointing, we applied correction for the frequency-dependent uGMRT primary beam model.³ In this process, we utilized 20% of the primary beam response to correct the image for each pointing. Subsequently, we used MONTAGE,⁴ to create a linear mosaic of the seven pointings, resulting in the one final combined image. In this process, each primary-beam corrected image is weighed by the square of the primary-beam pattern, which is considered proportional to the noise variance image. The overall mosaic of the ELAIS N1 field, covering an area of $\sim 0.8 \text{ deg}^2$, is depicted in Figure 1. Our analysis achieved a minimum central off-source RMS noise of $12 \mu\text{Jy beam}^{-1}$ with a beam size of $2''.3 \times 1''.9$.

2.4 Source catalog

In this study, we have used PyBDSF (Mohan & Rafferty 2015) software to create a catalog of sources and characterize them. We employed a sliding box window, `rms_box = (170, 40)`, on the final mosaicked image. To avoid counting bright artefacts as real sources, a

³<http://www.ncra.tifr.res.in/ncra/gmrt/gmrt-users/observing-help/uGMRT-primary-beam-shape>.

⁴<http://montage.ipac.caltech.edu/>.

smaller box of size (38, 8) was used around them. These bright regions are selected using an adaptive threshold of $150 \sigma_{\text{RMS}}$. P_VBDSF was then used to identify continuous regions of emission above a pixel threshold ($\text{thresh_pix} = 5\sigma$ and $\text{thresh_isl} = 3\sigma$) and model each region by fitting multiple Gaussian components.

Nearby Gaussian on the same island are grouped together to form a single source using P_VBDSF. Thus, total flux is measured as the sum of all the Gaussian fluxes, while the uncertainty is calculated by adding individual Gaussian uncertainties in quadrature. The position of the source is given by the centroid of the source. The PSF of the image may vary from its original value of the restoring beam. This is taken care by using the parameter `psf_vary_do = True`.

Using P_VBDSF, we generated a source catalog consisting of a total of 1086 sources above $>60 \mu\text{Jy}$ flux density (5σ). In Table 2, we list a sample of the source

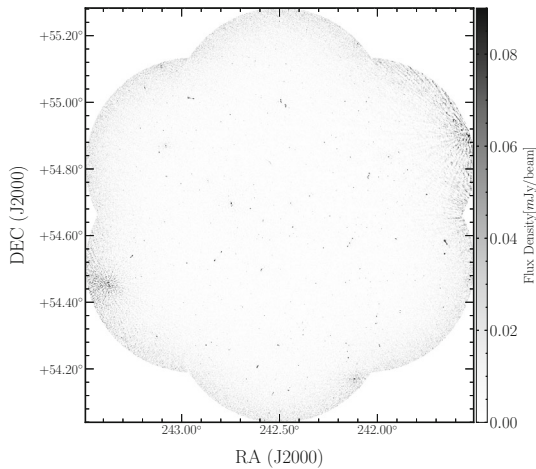


Figure 1. uGMRT mosaicked map of the ELAIS N1 field at 1.25 GHz with the central off-source RMS of $12 \mu\text{Jy beam}^{-1}$. The resolution of the image is $2''.3 \times 1''.9$.

catalog, while the complete catalog will be available with the electronic version of the paper. We have compared our catalog with other radio catalogs to investigate the positional and flux accuracies. This is discussed in Appendix A. We will discuss the point and resolve source identification in the following subsection.

2.5 Classification of sources

Because of various effects like time and bandwidth smearing, a source may get elongated in the image plane. Thus, making it difficult to identify the actual point and extended sources. For exceptional noise-free cases, the ratio of the integrated to the peak flux densities, $S_{\text{int}}/S_{\text{peak}} > 1$ can be used to identify resolved sources. Figure 2 presents the variation of $S_{\text{int}}/S_{\text{peak}}$ with S_{peak}/σ_1 , where σ_1 represents the local RMS here. It is assumed from the figure that the distribution is skewed at low SNR, which could be possible because of the noise variation and calibration uncertainties.

Following Franzen *et al.* (2015, 2019), we identified the resolved and point-like source in our sample. The RMS was estimated as:

$$\sigma_{\text{R}} = \sqrt{\left(\frac{\sigma_S}{S_{\text{int}}}\right)^2 + \left(\frac{\sigma_{S_{\text{peak}}}}{S_{\text{peak}}}\right)^2}. \quad (1)$$

Thus, a source is classified as resolved if $\ln(S/S_{\text{peak}}) > 3\sigma_{\text{R}}$ (Franzen *et al.* 2015). In this way, we identified 204 as extended and 882 sources as point-like from our 1250 MHz uGMRT catalog.

3. Source counts at 1.25 GHz

It is essential to understand the population distribution as a function of flux density, especially at low radio

Table 2. Sample of the source catalog at 1250 MHz from the uGMRT observations of ELAIS N1 field.

Id	RA (deg)	DEC (deg)	Total_flux (mJy)	Peak_flux (mJy beam ⁻¹)	Major (arcsec)	Minor (arcsec)	PA (degree)	RMS (mJy beam ⁻¹)
(1)	(2)	(3)	(4)	(5)	(6)	(7)	(8)	(9)
0	243.4352	54.6886	1.944	1.451	2.5	2.3	136.64	0.085
1	243.4006	54.5029	1.099	0.679	2.9	2.4	92.45	0.06
2	243.3881	54.4056	0.544	0.561	2.4	1.7	80.06	0.071
3	243.3811	54.4551	78.51	44.392	2.7	2.6	42.41	0.408
4	243.3793	54.4546	36.101	25.306	2.9	2.1	79.86	0.408

Note: The electronic version of the catalog is available, where the columns include the source ids, positions, flux densities and peak flux densities along with their respective errors. It also includes the sizes, position angle and the local RMS noise.

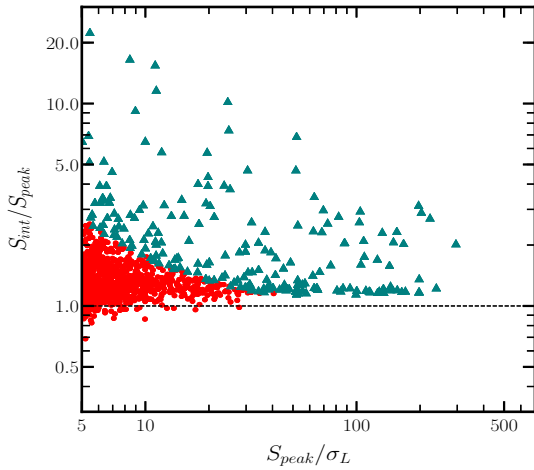


Figure 2. Variation in ratio of the integrated flux to the peak flux with the SNR of the source. The red and teal-colored sources represent the point and resolved sources, respectively.

frequencies. Further, it has been found from both observations (Padovani *et al.* 2015; Smolčić *et al.* 2017; Best *et al.* 2023) and simulations (Bonaldi *et al.* 2019) that the population of SFGs and RQ AGN dominate at faint fluxes. We have derived the normalized differential source counts for our uGMRT catalog at 1.25 GHz down to 60 μ Jy. However, direct measurement of source counts may have biases based on false detection rates (FDR), incompleteness, Eddington bias, etc. A few of these correction factors used, are briefly discussed below (following Williams *et al.* 2016).

3.1 FDR

There could be possible false detection of sources due to noise and artefacts in the PyBDSF compiled catalog. The total count of spurious detections is referred as false detection rates. Assuming a symmetrical distribution around zero, PyBDSF detected that spurious sources and negative sources (from inverted image) are equal. This can be quantified by running PyBDSF with the same parameters as applied for the original image. There were 20 sources with negative peaks less than the -5σ threshold. Following the method described in Hale *et al.* (2019), we measured the correction for each flux bin and multiplied the corresponding source count.

3.2 Completeness

The PyBDSF source catalog is not entirely complete due to factors that can lead to both overestimation and underestimation of source counts. Incompleteness refers to the inability to detect sources above a given

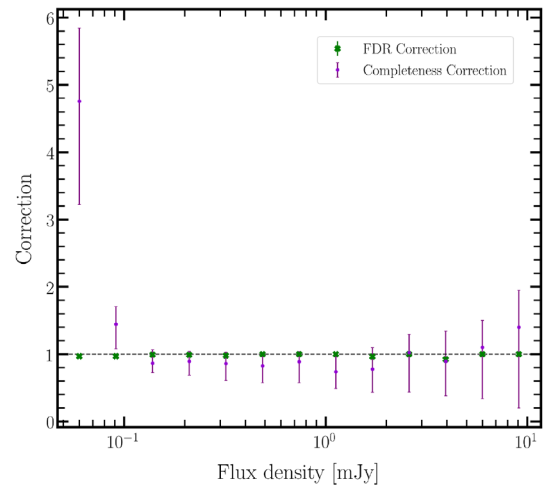


Figure 3. Correction factors are shown in green and purple for FDR and completeness, respectively.

flux density limit due to varying noise in the image. Eddington bias redistributes low flux density sources into higher fluxes, resulting in a boost in source counts in the faintest bins. Resolution bias reduces the detection probability of extended sources, leading to a reduction in source counts. The completeness of the catalog was quantified by injecting 800 sources, whose fluxes were derived as $dN/dS \propto S^{-1.6}$ (Intema *et al.* 2011; Williams *et al.* 2013), and into the primary beam-corrected image and extracting sources using PyBDSF. We have simulated these sources such that 650 are point sources, i.e., their major and minor axes lie in the range of $1.3''-2''$, while the remaining 150 are extended sources, i.e., major and minor axes are in the range of $2''-15''$. The sources are selected from a uniform distribution within these ranges. The ratio of the number of points and extended sources is taken nearly similar to that of the original 1.25 GHz catalog. Following the general trend of previous observations (Williams *et al.* 2016; Chakraborty *et al.* 2020; Mandal *et al.* 2021), we are within the uncertainty limits. This simulation was performed 100 times for robust estimation of the completeness factor. The completeness correction factor was calculated as the ratio of the number of injected sources with the number of recovered sources (Hale *et al.* 2019) for each flux bin, which accounts for both resolution bias and Eddington bias. Finally, the median values of the completeness factor from the 100 simulations in each flux bin are used to measure the completeness correction factor. Figure 3 shows the variation of correction factors due to FDR and completeness, which are with the flux bins in green and violet, respectively.

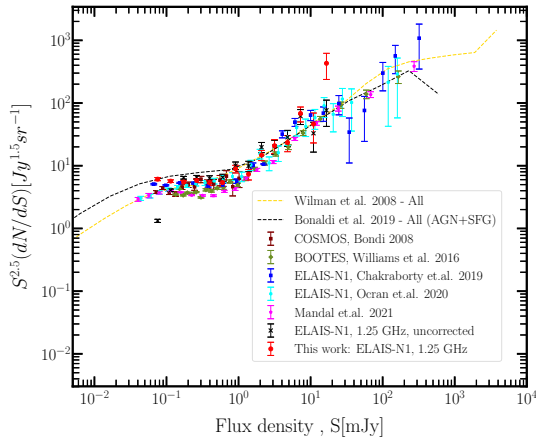


Figure 4. Euclidean differential source counts for the sources in the ELAIS N1 field using 1250 MHz uGMRT observations. The red points represent the corrected source counts here. The black crosses are the uncorrected source counts and are shown here only for comparison.

3.3 Differential source count

We obtained normalized differential source counts at 1250 MHz from the uGMRT catalog and adjusted for FDRs and completeness using correction factors for each flux bin. Figure 4 shows the corrected, normalized source counts in red points and the uncorrected counts in black crosses. We employed 11 logarithmically-spaced bins according to the flux density up to $60 \mu\text{Jy}$ (5σ). The errors estimated for the counts in each bin are Poisson errors.

In Figure 4, shows the source counts from various observations and simulations in the literature. All these values are scaled to 1250 MHz with $\alpha = -0.8$. Here, we have used the source counts for the same field, ELAIS N1 from Chakraborty *et al.* (2019) at 400 MHz and Ocran *et al.* (2020) at 610 MHz. The recent work by Mandal *et al.* (2021) is also shown, who have combined the LOFAR catalog at 150 MHz from the three fields, the ELAIS N1, the Boötes and Lockman Hole field. For comparison, we have also used the differential source counts from Bondi *et al.* (2008) for the COSMOS field and from Prandoni *et al.* (2018) for the Lockman Hole field, both at 1.4 GHz. Further, we used the S^3 -SKADS simulations (Wilman *et al.* 2008) and T-RECS simulations (Bonaldi *et al.* 2018), who have measured the source counts at 1.4 GHz.

Our measures of the differential source count at 1.25 GHz are consistent with the literature and flatten roughly around 1 mJy. At lower flux densities, it is observed that the counts at 1.25 GHz have a slight positive offset when compared to the results of Williams

et al. (2016) or Mandal *et al.* (2021). However, these are well within the boundary of the two simulations from SKADS and T-RECS. The mentioned simulations suggested an increase in the population of faint radio sources like SFGs and RQ AGN is reflected in the flattening of source counts below 1 mJy. Also, the recent observations from Sinha & Datta (under review) have confirmed the dominance of these source populations for the Bootes field using 400 MHz uGMRT observations. When compared at higher flux densities, the measured counts are consistent with sky models and observations.

4. Other radio continuum data

Our study has relied upon the source catalogs derived from radio observations of the ELAIS N1 field at three distinct frequencies further: 146 MHz obtained from LOFAR (Sabater *et al.* 2021), 400 MHz obtained from uGMRT (Chakraborty *et al.* 2019), and 612 MHz obtained from GMRT (Chakraborty *et al.* 2020). In this work, we have used the 400 MHz uGMRT catalog as the base catalog that contains 2528 sources above the 6σ threshold with point source sensitivity $\geq 100 \mu\text{Jy}$. The ELAIS N1 field was observed in the frequency range of 300–500 MHz and the final image reached an RMS noise of $15 \mu\text{Jy beam}^{-1}$ covering a sky area of 1.8 deg^2 . Chakraborty *et al.* (2019) describe the observations, calibration procedures and catalog generation in detail. Besides, we have also utilized the in-band catalogs centered at frequencies 325, 375, 425 and 475 MHz from Sinha *et al.* (2022), wherever available. We direct the reader to the specified references for a comprehensive account of the data analysis process and the catalog creation. These sources provide a detailed description of the methodology and procedures utilized in this study, offering a more in-depth understanding of the data analysis and catalog generation. We have used a search radius of 3 arcsec to determine the counterpart of sources in other catalogs except for 1250 MHz, where we have used a search radius of 2 arcsec. In Figure 5, we show the overlay of the uGMRT 1250 MHz catalog in red points with the 400 MHz catalog in blue points. Table 3 lists the salient features of the different surveys used in this work with their corresponding total number of 400 MHz uGMRT counterparts.

4.1 Redshifts and AGN/SFG classification

We have used the redshift information from BOSS spectroscopy (Bolton *et al.* 2012), the LOFAR photometric

redshifts (Duncan *et al.* 2021) and the SWIRE redshift catalog (Rowan-Robinson *et al.* 2013) for our purpose (see Sinha *et al.* 2022, for details). In this way, we have redshift information for 2319 sources in the 400 MHz uGMRT catalog. Moreover, we have used the classified sources as AGN (23.9%) and SFGs (76%) from Sinha *et al.* (2022) based on the BOSS spectroscopy, IRAC color classification, radio luminosity and observed q values, i.e., logarithmic of the ratio of luminosities in the infrared and radio wavebands. Here, it should be noted that the sources in 400 MHz catalog with redshift measurements are only considered for AGN/SFGs identification. All sources are classified as SFGs, which are not identified as AGN from the mentioned classification schemes.

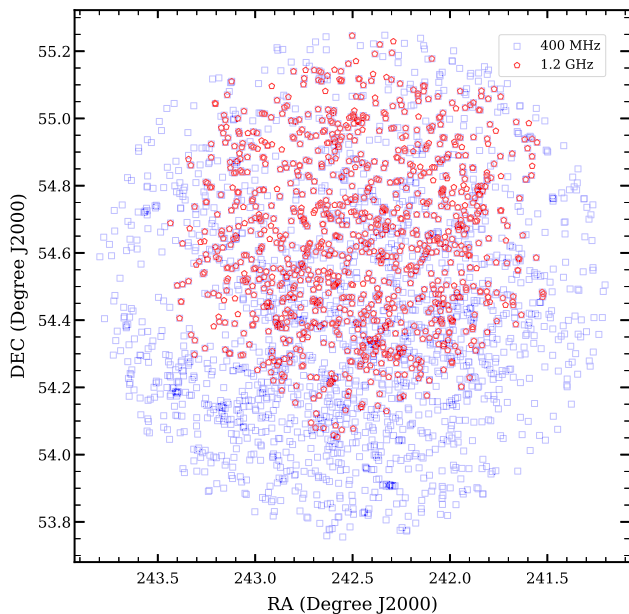


Figure 5. Source distribution in the ELAIS N1 field at 1.2 GHz in red and 400 MHz in blue using uGMRT.

5. Spectral properties

Spectral properties and radio SEDs offer valuable insights into the dominant emission mechanisms of different types of sources (Prandoni *et al.* 2010; Singh & Chand 2018). Spectral indices help us to classify the radio source populations at higher wavelengths. This information can be crucial in identifying and classifying various astrophysical sources, such as AGN, SFGs and radio relics, among others. A simple power-law model ($S \propto \nu^\alpha$) with negative α , implies the dominance of radio synchrotron emission commonly observed in radio galaxies. Whereas spectra with positive α are indicative of very young compact sources, also called peaked spectrum sources. Interestingly, an α value of ~ 0 suggests two possibilities: optically thick synchrotron emission in core-dominated AGN or optically thin free-free emission in SFGs that dominates at high frequencies ($\gtrsim 30$ MHz; Condon 1992). Therefore, by analysing the shape and characteristics of SEDs, it becomes possible to gain insights into the underlying physical processes driving the observed emission.

We performed a detailed analysis of the spectral properties for sources in the ELAIS N1 by comparing their flux densities at various radio frequencies. We assumed synchrotron power-law distribution with a single spectral index unless specified. Thus, the spectral index (α) are determined as:

$$\alpha = \frac{\log(S_1/S_2)}{\log(\nu_1/\nu_2)}, \tag{2}$$

where S_1 is the flux density at the frequency ν_1 and S_2 is the flux density at ν_2 . The focus of this section is to analyse the spectral features of the sources and classify them based on their spectral properties.

Table 3. Details of the catalogs considered. The columns represent the catalog, frequency in MHz, resolution, corresponding RMS noise and their 5σ sensitivity in mJy. The last two columns represent the total number of sources in a survey that have a counterpart in the 400 MHz uGMRT catalog and their corresponding percentages, respectively.

Catalogue	Frequency (MHz)	Resolution (arcsec)	σ (mJy)	S_{limit} (mJy)	Size	Percentage
uGMRT	400	4".5	0.015	0.075	2528 [†]	100
uGMRT	1250	2".0	0.012	0.06	853	34
LOFAR	150	6".0	0.02	0.10	2225	88
GMRT	612	6".0	0.008	0.04	1518	60

Note: Values in column 4, are the RMS noises as measured in the central region of the image. [†]All other catalogs are matched to these 2528 sources that are compiled above 6σ threshold (see Section 4).

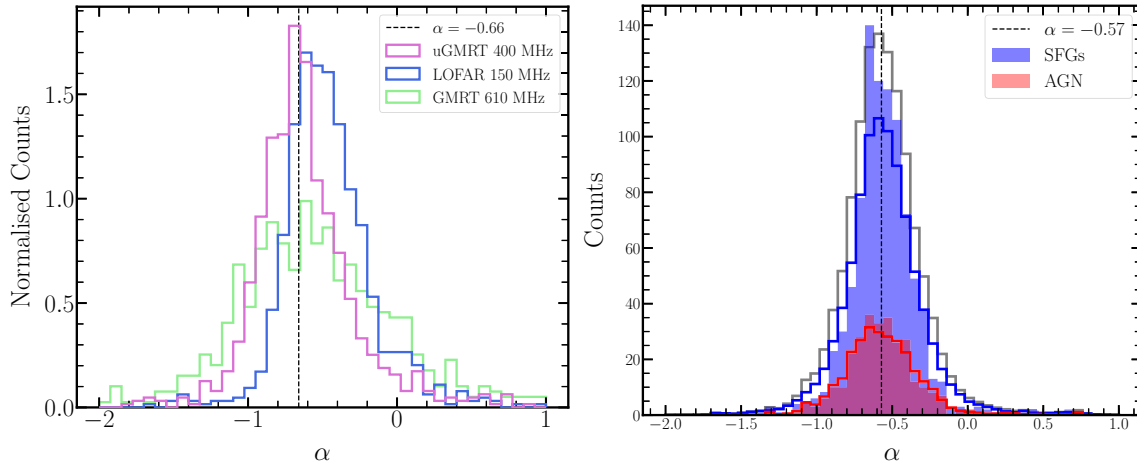


Figure 6. Spectral index distribution (see Section 5.1). Left: Obtained by measuring two-point spectral indices between 1250 MHz with 400, 146 and 612 MHz. Right: Derived by power-law fitting for each source. The dashed line indicates a median α value of -0.57 . The filled histograms present the distribution of SFGs and AGN in blue and red, respectively. While the open histograms denote the distribution obtained by accounting for the errors in α values.

5.1 Spectral index distribution

To analyse the spectral index distribution of the sources in the ELAIS N1 field, we calculated the two-point spectral indices (Equation 2) using 1.2 GHz with 400, 150 and 610 MHz. The total number of sources that matched with our L-band catalog to estimate spectral index distribution are: 853 (400 MHz uGMRT), 858 (150 MHz LOFAR) and 548 (610 MHz GMRT). Figure 6(left) shows the normalized histogram of the spectral indices estimated from the above-mentioned catalogs.

The median spectral value for the frequency range 400 MHz–1.2 GHz is -0.66 ± 0.17 and is shown with the black dashed line in the left panel of Figure 6. The median absolute deviation (MAD) is used to estimate the error on the median values for reference. We estimated median values, -0.50 ± 0.16 using 146 MHz–1.2 GHz and -0.58 ± 0.34 using 612 MHz–1.2 GHz, respectively.

Furthermore, we extended a similar analysis as described in [Sinha et al. \(2022\)](#) to measure the spectral indices by employing a power-law fit of the form $S \propto \nu^\alpha$. In brief, we divided the uGMRT data into four sub-bands between 300 and 500 MHz and ensured a minimum of three data points among all frequencies for robust SED fitting. Additionally, we conducted Monte Carlo simulations and drew 1000 random realizations for each frequency to account for flux density uncertainties. Each realization is then fitted to obtain 1000 α values with the mean calculated as the α value for each source. Figure 6(right-panel) illustrates the α distribution for the sample of uGMRT sources in gray with SFGs and AGN identified in [Sinha et al. \(2022\)](#) shown

in blue and red, respectively. The median α value for all sources was -0.57 ± 0.14 with median values of 0.58 ± 0.13 and -0.59 ± 0.14 for SFGs and AGN, respectively. These results are consistent with previous findings and support the trend of flattening spectral indices at lower frequencies, as reported in [Coppejans et al. \(2015\)](#) and other relevant literature ([An et al. 2023](#)).

5.2 Spectral classification

We have generated a radio color plot for 697 sources located in the ELAIS N1 field, which have matched in all four catalogs at frequencies: 146, 400, 612 and 1250 MHz and is displayed in Figure 7. To prevent any ambiguity, the plot does not show error bars. However, the median errors for α_{146}^{612} and α_{400}^{1250} are available as a reference with values of 0.10 and 0.22, respectively. We have used the two-point spectral indices between 146 and 610 MHz, and between 400 MHz and 1.25 GHz to classify the sources into four spectral categories:

1. Steep and flat ($\alpha_{400}^{1250} \leq 0$ and $\alpha_{146}^{612} \leq 0$),
2. Peaked ($\alpha_{400}^{1250} \leq 0$ and $\alpha_{146}^{612} > 0$),
3. Inverted ($\alpha_{400}^{1250} > 0$ and $\alpha_{146}^{612} > 0$),
4. Upturning ($\alpha_{400}^{1250} > 0$ and $\alpha_{146}^{612} \leq 0$).

As evident, more sources lie in the steep and flat spectrum quadrant. Sources in the inverted quadrant are likely to be dominated by GPS or HFP sources, whose spectral peaks lie at higher frequencies $\gtrsim 1$ GHz. The peaking quadrant consists of the sources whose turnover

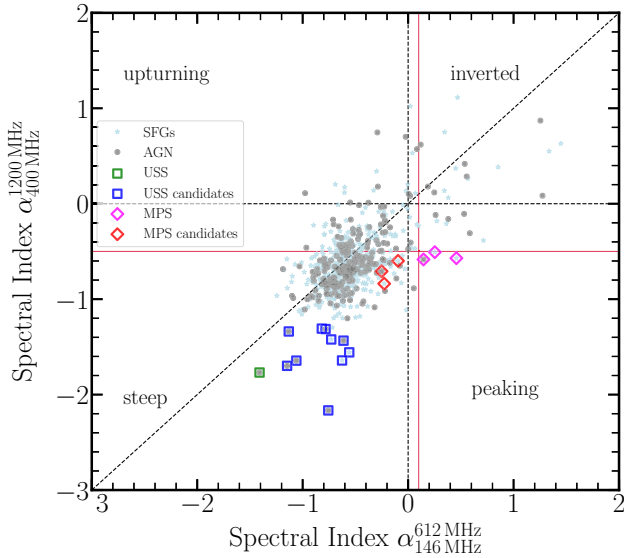


Figure 7. Radio color–color diagram where SFGs are represented by light-blue star symbols, and AGN are indicated by gray circle symbols. The figure is divided into four quadrants with dashed black lines that represent sources that may have upturning, inverted, steepening and peaking properties in their spectra (see Section 5.2). The red lines represent spectral index limits used to identify the MPS sources in the field. The open squares and open diamonds represent USS and MPS sources, respectively (see text for details).

frequency lie within the frequency range of 400–1400 MHz and is discussed in Section 5.2.2. The upturning quadrant comprises the composite sources that have a steep power-law spectrum at low frequencies and an inverted spectrum at high frequencies. Thus, this could be an indication of multiple epochs of AGN activity.

The majority of sources (~92%) belong to the steep spectrum quadrant, and out of these, 29.5% are AGN, while the rest are SFGs. Out of the total 213 AGN shown in the figure, this steep quadrant covers almost 89% of the AGN population and is consistent with the properties of RL AGN. In the following subsections, we discuss the properties of USS and MPS sources in detail.

5.2.1 Ultra steep spectrum sources High-redshift radio galaxies (HzRGs; $z > 2$) are often observed in the early Universe and are typically located in the midst of protoclusters within regions of high density (Roettgering *et al.* 1994; Knopp & Chambers 1997). These overdense regions are conducive to galaxy formation and growth, making them an important target to study the early stages of galaxy evolution and the physical processes driving them. HzRGs are thought to be the predecessors of the massive elliptical galaxies that are observed in the local Universe. USS tend

to be favorable candidates for HzRGs with extremely steep spectral indices (Blundell *et al.* 1998; Miley & De Breuck 2008; Riseley *et al.* 2016). Different studies in the literature have used various selection limits on the spectral indices; for instance, Blundell *et al.* (1998) used $\alpha_{151 \text{ MHz}}^{4.5 \text{ GHz}} < -0.981$, De Breuck *et al.* (2004): $\alpha_{843 \text{ MHz}}^{1.4 \text{ GHz}} < -1.3$ and Singh *et al.* (2014): $\alpha_{325 \text{ MHz}}^{1.4 \text{ GHz}} < -1.0$. The very steep alpha values observed in these sources are believed to be a result of radiation losses in the radio lobes from relativistic electrons (Mahony *et al.* 2016b), indicating that these sources are highly luminous at lower frequencies.

In this study, we employed the spectral limit of $\alpha < -1.3$ to identify USS sources from our sample in the ELAIS N1 field. The first method we used, involved performing the SED fitting for the sources (see Section 5.1), while the second method involved using the radio color plot to identify USS sources. We were able to identify nine USS sources in our 400 MHz catalog with the SED fitting method. Table 4 presents the list of USS sources identified in this way. Out of these, one is identified as AGN, while eight as SFGs from our previous analyses. Meanwhile, using the radio-color plot, we classified one source as a USS source, which was already identified through the SED fitting method. This source is shown as the open green square in Figure 7, and the spectra of all the nine sources are attached to Appendix B. It is noted that excluding two sources, all the remaining sources in our study exhibit redshift values < 1 .

Besides, there are 10 other sources for which $\alpha_{400 \text{ MHz}}^{1.25 \text{ GHz}} < -1.3$ and are shown as open blue squares in Figure 7. Nevertheless, the alpha values obtained for these sources from the SED fitting are distributed in the redshift range of 0.17–3.19. These could be potential USS sources in our uGMRT sample and the details of which are listed in Table 5.

5.2.2 Megahertz peaked spectrum sources We employed the radio color–color plot to identify sources with multiple power-law spectra in the ELAIS N1 field. Our criteria to select peaked spectrum sources are $\alpha_{\text{low}} > 0.1$ and $\alpha_{\text{high}} < -0.5$ (Callingham *et al.* 2017), where α_{low} and α_{high} correspond to the spectral indices between 146 and 612 MHz, and between 400 MHz and 1.25 GHz, respectively. The above limit is used to avoid contamination of flat spectrum sources and thus, make the selection more reliable. Figure 7 shows the red lines indicating the criteria used to identify the MPS sources. We successfully identified three sources meeting these criteria and have listed their details along with their respective redshifts in the first three rows of Table 6.

Table 4. Ultra-steep spectrum sources obtained by SED fitting. The ID column represents the source ID from the 400 MHz uGMRT catalog. The spectral indices obtained by the power-law fit (α_{fit}) method and from the Monte Carlo method (α_{MC}) are also mentioned along with their redshifts in the last column.

ID	RA	DEC	α_{fit}	α_{MC}	z
50	243.6005	54.7216	-1.65 ± 0.04	-1.65 ± 0.03	0.34
1180	242.5347	54.3207	-1.30 ± 0.13	-1.32 ± 0.13	1.02
1335	242.4393	53.8292	-1.38 ± 0.69	-1.40 ± 0.70	0.63
1344	242.4347	53.9631	-1.79 ± 0.13	-1.79 ± 0.16	0.72
1400	242.3979	54.0800	-1.35 ± 0.58	-1.33 ± 0.93	0.32
1452	242.3678	54.3307	-1.42 ± 0.23	-1.42 ± 0.06	0.76
1544	242.3142	54.2309	-1.31 ± 0.07	-1.31 ± 0.01	2.60
2150	241.9042	54.1795	-1.46 ± 0.14	-1.46 ± 0.09	0.49
2480	241.4090	54.6925	-1.37 ± 0.09	-1.38 ± 0.06	0.24

Table 5. Details of the potential USS source in the ELAIS N1 field.

ID	RA	DEC	$\alpha_{400 \text{ MHz}}^{1.2 \text{ GHz}}$	z
2074	241.9562	54.8896	-1.31 ± 0.27	0.17
194	243.3113	54.2970	-1.64 ± 0.10	2.87
344	243.1391	54.9420	-1.42 ± 0.19	0.08
2379	241.6505	54.5475	-1.34 ± 0.06	1.33
354	243.1264	54.8527	-2.17 ± 0.07	0.39
966	242.6523	54.6856	-1.43 ± 0.04	1.65
284	243.2046	55.0445	-1.64 ± 0.07	0.49
1316	242.4478	54.3250	-1.56 ± 0.27	0.34
479	243.0141	54.5015	-1.31 ± 0.36	0.45
1896	242.0792	54.8541	-1.70 ± 0.27	3.19

Moreover, in addition to the criteria based on the radio color plot, we visually examined the power-law fits (Section 5.1) of individual sources. This analysis led us to identify three more sources with spectral peaks at mega-hertz frequencies, which are not evident from the radio color plot. The relevant information about these sources, along with their redshifts, is summarized in the bottom three rows of Table 6. To perform spectral fitting on these sources separately, we utilized the generic model described in Callingham *et al.* (2017):

$$S_\nu = \frac{S_p}{(1 - e^{-1})} (1 - e^{(\nu/\nu_p)^{\alpha_{\text{thin}} - \alpha_{\text{thick}}})} (\nu/\nu_p)^{\alpha_{\text{thick}}}, \quad (3)$$

where S_p is the peak flux density at the peak frequency (ν_p), α_{thick} and α_{thin} are the spectral indices in the optically thick and thin regimes of the spectrum, respectively.

The top-panel of Figure 8 displays the observed spectrum of the source with ID 1155 at a redshift of 0.01. As depicted from the image of Figure 8, it is a compact

source at 400 MHz. The measured peak frequency of this source is 152.4 ± 4.01 MHz, while the values of the spectral indices α_{thick} and α_{thin} are 3.35 ± 1.17 and -0.62 ± 0.02 , respectively.

Also, the middle and bottom panels of Figure 8 present the fitted spectra for sources with ID 595 and 1194 and having their peak frequencies around 158.29 ± 24.48 MHz and 168.07 ± 28.69 MHz, respectively. These sources are also compact and detected at redshifts of 0.18 and 1.04.

The MPS sources identified in this study were found to span a redshift range of $0.01 < z < 3.38$, with only one source having spectroscopic redshift information. This range suggests that these sources could potentially be young AGN at higher redshifts. It has been previously reported that MPS sources can encompass a combination of nearby CSS and GPS, and HFP sources at high redshifts (Coppejans *et al.* 2015). This is also likely the case for the sources included in our study. The parameters derived for the three MPS sources using

Table 6. Details of the MPS sources in the ELAIS N1 field. The top three rows in the table represent MPS sources that were identified using the radio color diagram. On the other hand, the bottom three sources correspond to MPS sources that were selected based on visual inspection from the SED fits.

ID	RA (deg)	DEC (deg)	z
1022	242.62222	54.92758	0.267
1925	242.05520	55.00188	1.74
2162	241.89594	54.55692	3.38
1155	242.55263	54.59195	0.013
595	242.91821	54.24502	0.18
1194	242.52626	54.30840	1.04

Equation (1) are similar to those presented in [Keim et al. \(2019\)](#), where the authors suggest FFA as the most likely absorption mechanism based on the source’s peak frequencies, linear sizes and magnetic field. Therefore, it is possible that the bottom three sources in [Table 6](#) also exhibit FFA as the absorption mechanism. However, more data are required at the low frequencies to get robust SED fitting parameters and therefore, to comprehend the physical mechanism responsible for the observed peaked spectra. On the other hand, it is also important to note that for the SSA mechanism to occur, the spectral slope cannot cross the threshold of $+2.5$ below the turnover and therefore, FFA has been the widely suggested mechanism for any such scenarios (see e.g., [Bicknell et al. 1997](#); [Callingham et al. 2015](#)).

5.3 Radio spectral index vs. redshift

It is believed that there lies a strong anti-correlation between the spectral index and redshift of the radio sources ([Athreya & Kapahi 1999](#); [Miley & De Breuck 2008](#)). The study of $z \sim \alpha$ correlation has been used to search for high-redshift radio galaxy (HzRG) candidates in large area radio surveys (see e.g., [Roettgering et al. 1997](#)). The plausible explanations of $z \sim \alpha$ correlation i.e., the steepness of spectral index with redshift, are as follows: (a) K-correction: In the case of high redshift sources, the spectrum experiences a shift towards lower frequencies, resulting in the inclusion of the steep portion within the observed spectrum. (b) Indirect manifestation of luminosity, $L \sim \alpha$ effect ([Chambers et al. 1990](#)). (c) Density-dependent effect: The ambient density increases at higher redshifts; thus, jets from radio sources have to move against the surrounding denser medium, which in turn gives rise to strong synchrotron losses at higher frequencies.

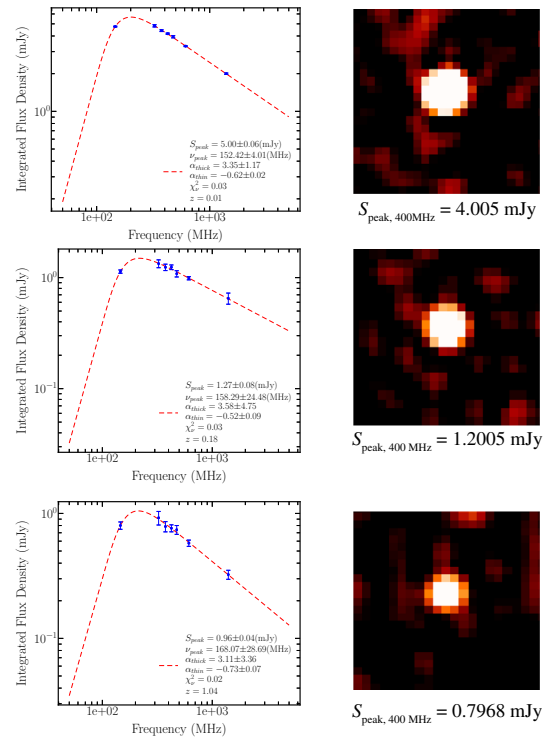


Figure 8. Spectral energy distribution (left) for three MPS sources (source IDs 1155, 595 and 1194 in [Table 6](#)) shown at 400 MHz on the right. The $S_{\text{peak}, 400 \text{ MHz}}$ represents the peak flux values for these images at 400 MHz.

The studies by [Morabito & Harwood \(2018\)](#) in radio galaxies suggested that the observed $z \sim \alpha$ relation could be explained by the possibility of combining the selection effects and inverse Compton losses at high redshifts. Whereas, [Saxena et al. \(2019\)](#) studied a sample of 32 USS sources and found no strong anti-correlation between z and α among their sample.

We studied the observed correlation between radio spectral index and redshift for the sources in the ELAIS N1 field. [Figure 9](#) represents the variation of radio spectral index with redshift for AGN (gray circles), SFGs (light-blue stars) and USS sources (open green squares). Here, the spectral indices used are the ones derived using the SED fits. The Pearson correlation coefficient (r) for the SFGs, AGN and USS sources in [Figure 9](#) are 0.08, -0.15 and 0.28, respectively. We do not find any strong anti-correlation for the radio sources in the ELAIS N1 field. The limited number of USS samples that we obtained from the field indicate no observable changes in spectral indices as redshift increases.

Besides, the SFGs sample shows an almost negligible variation of spectral indices with redshift. This is consistent with the analyses of [Iverson et al. \(2010\)](#), [Magnelli et al. \(2015\)](#) and [Calistro et al. \(2017\)](#). The

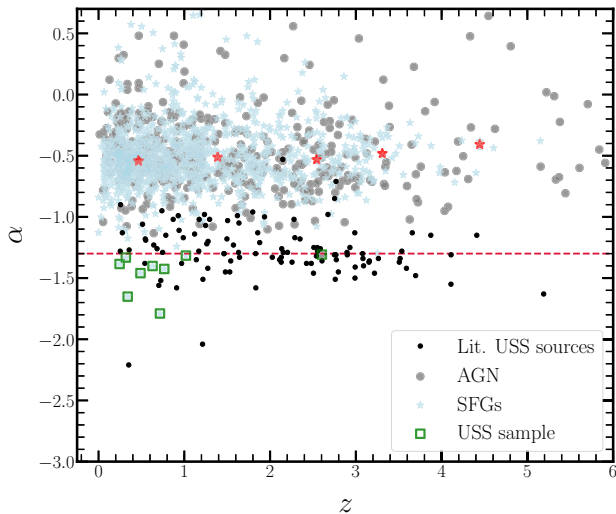


Figure 9. Radio spectral index as a function of redshift for the SFGs, AGN and USS sources in the ELAIS N1. The red dashed line represents $\alpha = -1.3$, the criterion adopted to identify USS sources.

red star symbols depicted in Figure 9 correspond to the median values of SFGs across five redshift bins. This non-evolution of spectral values with redshift suggests that the radio spectrum is independent of the properties of the galaxies in the large-scale context, where redshift evolution plays a major role. This further implies that the local properties of the galaxies like magnetic fields, surrounding interstellar medium (ISM) and cosmic ray electrons (CREs) from the supernova contribute to the nature of radio SED.

6. Discussion and summary

In this study, we focused on the ELAIS N1 field of the deep extra-galactic sky and analysed it at 1250 MHz using the uGMRT. We reached an RMS noise of $\sim 12 \mu\text{Jy beam}^{-1}$ and cataloged 1086 sources at this frequency. Given that the ELAIS N1 field has been widely explored at various frequencies, we cross-matched our uGMRT sample at 400 MHz with other catalogs to investigate their various spectral properties.

From our analyses of the radio SED fits, we determined the median spectral index value for our uGMRT sample to be $\alpha = -0.57 \pm 0.14$, which implies the flattening of radio spectral values at low frequencies. Whereas, the median value of the two-point spectral indices measured between the frequency of 400 and 1250 MHz is $\alpha_{400}^{1250} = -0.66 \pm 0.17$. After cross-matching sources in the uGMRT 400 MHz with other radio catalogs at different frequencies, we found that the majority of the sample belongs to the steep spectrum

quadrant with less number of sources in other quadrants, as depicted in Figure 7. This figure presents the radio color diagram for SFGs and AGN, the classification of which is obtained from [Sinha et al. \(2022\)](#) at 400 MHz. Based on the spectral indices measured by employing the SED fits, we identified nine USS sources in the redshift range of 0.24–2.60.

Furthermore, based on the radio color diagram, we classify three sources as MPS sources. Moreover, three additional sources were visually selected due to their exhibited peaked spectra at MHz frequencies. A general SED fit was performed to determine their peaked frequencies that lie around 152, 158 and 168 MHz. The measured spectral slope below the turnover for all three sources is found to be $\alpha_{\text{thick}} > 3.1$. This value indicates that the FFA mechanism is the plausible explanation for the observed spectra in these cases, but for a detailed analysis, more data are required, especially below the spectral turnover.

Finally, in our study, we present the analysis of spectral indices (obtained through SED fitting) and their correlation with redshifts for three distinct source categories: SFGs, AGN and USS sources. We observe a lack of strong anti-correlation among the radio sources in the ELAIS N1 field. Especially for SFGs, this may mean that the nature of the radio SED is mostly dependent on the local parameters within the galaxies, like magnetic fields, properties of the surrounding ISM, etc. and is independent of the properties in the large-scale context for which redshift evolution becomes crucial.

Acknowledgements

We thank the anonymous referee for their comments on the manuscript. We further would like to thank Arnab Chakraborty for his helpful suggestions. AS would like to thank DST for INSPIRE fellowship. We thank the staff of GMRT for making this observation possible. GMRT is run by National Centre for Radio Astrophysics of the Tata Institute of Fundamental Research.

Appendix A. Positional and flux accuracies

Here, we compare the uGMRT 1.25 GHz catalog to the other radio catalogs in the literature. We have used the 1.4 GHz Faint Images of the Radio Sky at Twenty centimeters (FIRST) survey ([White et al. 1997](#)), uGMRT catalog at 400 MHz from (for details, see Section 4, [Chakraborty et al. 2019](#)) the GMRT catalog at 610 MHz by [Ishwara-Chandra et al. \(2020\)](#) with the resolution of $6''$. We used a search radius of $2''.0$ to

identify a cross-match in other catalogs. For the positional and flux accuracy analysis, we have applied a sample selection criteria of sources following [Williams et al. \(2016\)](#): High signal-to-noise ratio (>10) sources, compact sources with size less than the resolution of the catalog and isolated sources for which the minimum distance between the two sources are greater than twice of the resolution.

Appendix A.1 Positional accuracy

The positional offsets in right ascension (RA) and declination (DEC) for the uGMRT sample at 1.25 GHz are measured as:

$$\delta_{\text{RA}} = \text{RA}_{\text{uGMRT}} - \text{RA}_{\text{FIRST}}, \quad (\text{A1})$$

$$\delta_{\text{DEC}} = \text{DEC}_{\text{uGMRT}} - \text{DEC}_{\text{FIRST}}. \quad (\text{A2})$$

The FIRST catalog has positional accuracy better than $1''$ with a resolution of $\sim 5''$. We measured the median values in the deviation of RA and DEC using the FIRST catalog as $-0.092''$ and $-0.076''$, respectively. Figure 10(left) presents the offsets in RA and DEC for the uGMRT source catalog compared to the other catalogs, along with their histograms. The median offsets in RA and DEC, as measured from the GMRT 610 MHz and the uGMRT 400 MHz catalogs, are -0.07 , -0.16 and

-0.43 , 0.59 , respectively. It should be noted that the resolution of our catalog $\sim 2''$ is better than the resolution of other catalogs $\sim 5''-6''$, and the median offset with the FIRST catalog is $<0.1''$. Hence, we do not apply any corrections in the source positions in our uGMRT catalog.

Appendix A.2 Flux accuracy

Our uGMRT 1.25 GHz catalog was generated using [Perley & Butler \(2017\)](#) flux scales. Each catalog will have different flux scales, therefore, we have made sure to convert them to the flux scales used in our work. We measured the ratio of the integrated flux density at 1.25 GHz with the other catalogs also scaled to 1.25 GHz using a constant spectral index value of -0.7 . This ratio is defined as $S_{1.25 \text{ GHz}}/S_{\text{other}}$. In Figure 10(right), we show the comparison of $S_{1.25 \text{ GHz}}$ with S_{other} and no significant deviation is observed from the $S_{1.25 \text{ GHz}}/S_{\text{other}} = 1$ line (black dashed line). The median $S_{1.25 \text{ GHz}}/S_{\text{other}}$ ratio as derived using the FIRST, uGMRT 400 MHz and GMRT 610 MHz catalogs are $0.99^{0.19}_{-0.37}$, $1.11^{0.25}_{-0.51}$ and $1.10^{0.32}_{-0.9}$, respectively. The errors quoted here are from the 16th and 84th percentiles. The median of the ratio is ~ 1 for these cases and therefore, we do not suggest any correction for systematic offsets.

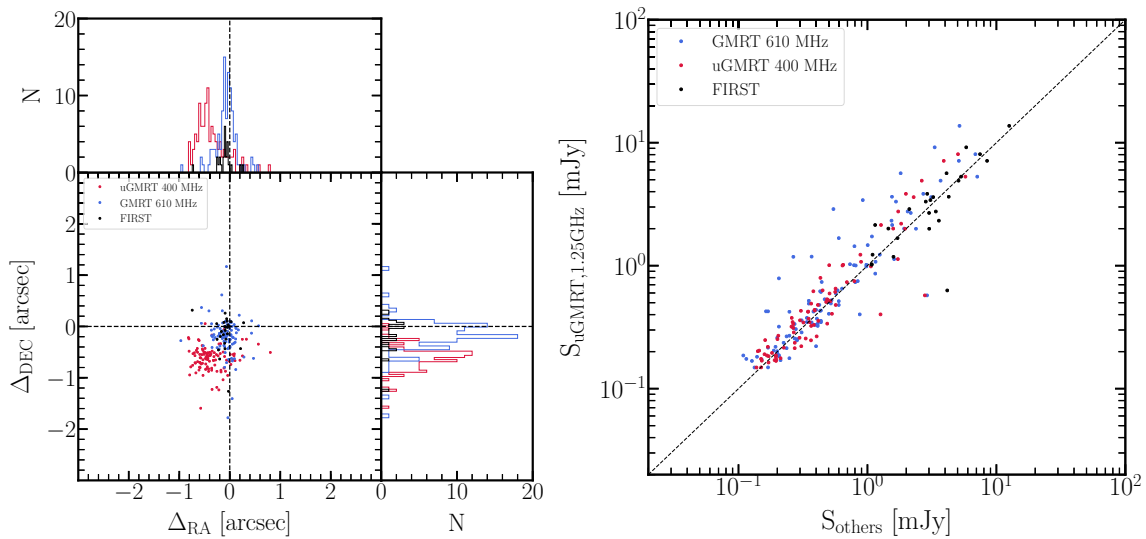


Figure 10. Left: Positional offset for the uGMRT sample at 1.25 GHz from FIRST (black), GMRT 610 MHz (blue) and uGMRT 400 MHz (red) catalogs. Right: Variation of integrated flux densities at 1.25 GHz with other radio catalogs scaled to this frequency. The color schemes are same as in the left panel.

Appendix B. Spectra of USS sample

The spectra of the USS sources are shown in Figure 11.

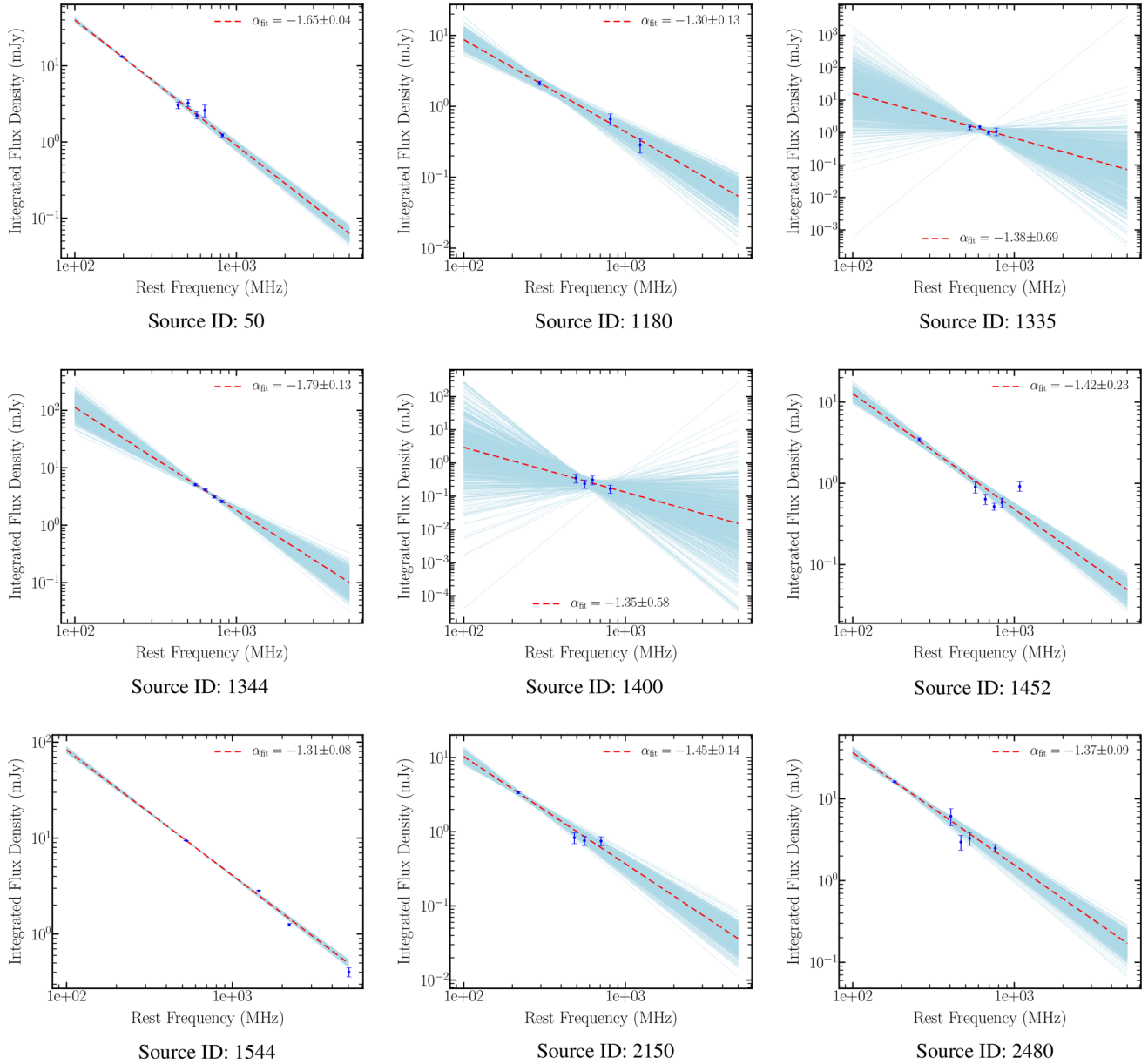


Figure 11. Spectra for the USS sources in the ELAIS N1 field. The source IDs mentioned here are from the 400 MHz uGMRT catalog.

References

- An F., Vaccari M., Best P. N. *et al.* 2023, arXiv e-prints, [arXiv:2303.06941](https://arxiv.org/abs/2303.06941)
- An T., Baan W. A. 2012, *Astrophysical Journal*, 760, 77
- Athreya R. M., Kapahi V. K. 1999, in ed Sato K., IAU Symposium, Vol. 183, *Cosmological Parameters and the Evolution of the Universe*, p. 251
- Best P. N., Arts J. N., Röttgering H. J. A. *et al.* 2003, *Monthly Notices of the Royal Astronomical Society*, 346, 627
- Best P. N., Kondapally R., Williams W. L. *et al.* 2023, *Monthly Notices of the Royal Astronomical Society*, 523, 1729
- Bicknell G. V., Dopita M. A., O’Dea C. P. O. 1997, *The Astrophysical Journal*, 485, 112
- Bicknell G. V., Mukherjee D., Wagner A. Y., Sutherland R. S., Nesvadba N. P. H. 2018, *Monthly Notices of the Royal Astronomical Society*, 475, 3493
- Blundell K. M., Kuncic Z. 2007, *Astrophysical Journal Letters*, 668, L103
- Blundell K. M., Rawlings S., Eales S. A., Taylor G. B., Bradley A. D. 1998, *Monthly Notices of the Royal Astronomical Society*, 295, 265
- Bolton A. S., Schlegel D. J., Aubourg É. *et al.* 2012, *The Astronomical Journal*, 144, 144
- Bonaldi A., Bonato M., Galluzzi V. *et al.* 2019, *Monthly Notices of the Royal Astronomical Society*, 482, 2
- Bonaldi A., Bonato M., Galluzzi V. *et al.* 2018, *Monthly Notices of the Royal Astronomical Society*, 482, 2
- Bondi M., Ciliegi P., Schinnerer E. *et al.* 2008, *Astrophysical Journal*, 681, 1129
- Bonzini M., Padovani P., Mainieri V. *et al.* 2013, *Monthly Notices of the Royal Astronomical Society*, 436, 3759
- Calistro R. G., Williams W. L., Hardcastle M. J. *et al.* 2017, *Monthly Notices of the Royal Astronomical Society*, 469, 3468
- Callingham J. R., Gaensler B. M., Ekers R. D. *et al.* 2015, *The Astrophysical Journal*, 809, 168
- Callingham J. R., Ekers R. D., Gaensler B. M. *et al.* 2017, *Astrophysical Journal*, 836, 174
- Chakraborty A., Dutta P., Datta A., Roy N. 2020, *Monthly Notices of the Royal Astronomical Society*, 494, 3392
- Chakraborty A., Roy N., Datta A. *et al.* 2019, *Monthly Notices of the Royal Astronomical Society*, 490, 243
- Chambers K. C., Miley G. K., van Breugel W. J. M. 1990, *Astrophysical Journal*, 363, 21
- Condon J. J. 1992, *Annual Review of Astron and Astrophys*, 30, 575
- Coppejans R., Cseh D., Williams W. L., van Velzen S., Falcke H. 2015, *Monthly Notices of the Royal Astronomical Society*, 450, 1477
- Coppejans R., Cseh D., van Velzen S. *et al.* 2016, *Monthly Notices of the Royal Astronomical Society*, 459, 2455
- De Breuck C., Hunstead R. W., Sadler E. M., Rocca-Volmerange B., Klamer I. 2004, *VizieR Online Data Catalog*, J/MNRAS/347/837
- Duncan K. J., Kondapally R., Brown M. J. I. *et al.* 2021, *Astronomy & Astrophysics*, 648, A4
- Fabian A. C. 2012, *Annual Review of Astron and Astrophys*, 50, 455
- Franzen T. M. O., Vernstrom T., Jackson C. A. *et al.* 2019, *Publications of the Astron. Soc. of Australia*, 36, e004
- Franzen T. M. O., Banfield J. K., Hales C. A. *et al.* 2015, *Monthly Notices of the Royal Astronomical Society*, 453, 4020
- Hale C. L., Williams W., Jarvis M. J. *et al.* 2019, *Astronomy & Astrophysics*, 622, A4
- Hardcastle M. J., Williams W. L., Best P. N. *et al.* 2019, *Astronomy & Astrophysics*, 622, A12
- Intema H. T., van Weeren R. J., Röttgering H. J. A., Lal D. V. 2011, *Astronomy & Astrophysics*, 535, A38
- Ishwara-Chandra C. H., Taylor A. R., Green D. A. *et al.* 2020, *Monthly Notices of the Royal Astronomical Society*, 497, 5383
- Ivison R. J., Alexander D. M., Biggs A. D. *et al.* 2010, *Monthly Notices of the Royal Astronomical Society*, 402, 245
- Keim M. A., Callingham J. R., Röttgering H. J. A. 2019, *Astronomy & Astrophysics*, 628, A56
- Knopp G. P., Chambers K. C. 1997, *The Astrophysical Journal*, 487, 644
- Magnelli B., Ivison R. J., Lutz D. *et al.* 2015, *Astronomy & Astrophysics*, 573, A45
- Mahony E. K., Morganti R., Prandoni I., van Bemmel I., LOFAR Surveys Key Science Project. 2016a, *Astronomische Nachrichten*, 337, 135
- Mahony E. K., Morganti R., Prandoni I. *et al.* 2016, *Monthly Notices of the Royal Astronomical Society*, 463, 2997
- Mandal S., Prandoni I., Hardcastle M. J. *et al.* 2021, *Astronomy & Astrophysics*, 648, A5
- Miley G., De Breuck C. 2008, *Astronomy and Astrophysics Reviews*, 15, 67
- Miller P., Rawlings S., Saunders R. 1993, *Monthly Notices of the Royal Astronomical Society*, 263, 425
- Mohan N., Rafferty D. 2015, *PyBDSF: Python Blob Detection and Source Finder Astrophysics Source Code Library*, ascl:1502.007
- Morabito L. K., Harwood J. J. 2018, *Monthly Notices of the Royal Astronomical Society*, 480, 2726
- Murgia M., Fanti C., Fanti R. *et al.* 1999, *Astronomy & Astrophysics*, 345, 769
- Ocran E. F., Taylor A. R., Vaccari M., Ishwara-Chandra C. H., Prandoni I. 2020, *Monthly Notices of the Royal Astronomical Society*, 491, 1127
- O’Dea C. P. 1998, *Publications of the ASP*, 110, 493
- O’Dea C. P., Baum S. A. 1997, *Astronomical Journal*, 113, 148
- Offringa A. R., Smirnov O. 2017, *Monthly Notices of the Royal Astronomical Society*, 471, 301
- Offringa A. R., McKinley B., Hurley-Walker N. *et al.* 2014, *Monthly Notices of the Royal Astronomical Society*, 444, 606

- Orienti M. 2016, *Astronomische Nachrichten*, 337, 9
- Orienti M., Dallacasa D., Tinti S., Stanghellini C. 2006, *Astronomy & Astrophysics*, 450, 959
- Padovani P. 2016, in *Active Galactic Nuclei 12: A Multi-Messenger Perspective (AGN12)*, p. 14
- Padovani P., Bonzini M., Kellermann K. I. *et al.* 2015, *Monthly Notices of the Royal Astronomical Society*, 452, 1263
- Padovani P., Mainieri V., Tozzi P. *et al.* 2009, *Astrophysical Journal*, 694, 235
- Padovani P., Miller N., Kellermann K. I. *et al.* 2011, *Astrophysical Journal*, 740, 20
- Panessa F., Baldi R. D., Laor A. *et al.* 2019, *Nature Astronomy*, 3, 387
- Perley R. A., Butler B. J. 2017, *The Astrophysical Journal Supplement Series*, 230, 7
- Prandoni I., de Ruiter H. R., Ricci R. *et al.* 2010, *Astronomy & Astrophysics*, 510, A42
- Prandoni I., Guglielmino G., Morganti R. *et al.* 2018, *Monthly Notices of the Royal Astronomical Society*, 481, 4548
- Riseley C. J., Scaife A. M. M., Hales C. A. *et al.* 2016, *Monthly Notices of the Royal Astronomical Society*, 462, 917
- Roettgering H. J. A., Lacy M., Miley G. K., Chambers K. C., Saunders R. 1994, *A&AS*, 108, 79
- Roettgering H. J. A., van Ojik R., Miley G. K. *et al.* 1997, *Astronomy & Astrophysics*, 326, 505
- Rowan-Robinson M., Gonzalez-Solares E., Vaccari M., Marchetti L. 2013, *Monthly Notices of the Royal Astronomical Society*, 428, 1958
- Sabater J., Best P. N., Tasse C. *et al.* 2021, *Astronomy & Astrophysics*, 648, A2
- Saxena A., Röttgering H. J. A., Duncan K. J. *et al.* 2019, *Monthly Notices of the Royal Astronomical Society*, 489, 5053
- Singh V., Chand H. 2018, *Monthly Notices of the Royal Astronomical Society*, 480, 1796
- Singh V., Beelen A., Wadadekar Y. *et al.* 2014, *VizieR Online Data Catalog*, J/A+A/569/A52
- Sinha A., Basu A., Datta A., Chakraborty A. 2022, *Monthly Notices of the Royal Astronomical Society*, 514, 4343
- Smolčić V., Schinnerer E., Scodreggio M. *et al.* 2008, *ApJS*, 177, 14
- Smolčić V., Delvecchio I., Zamorani G. *et al.* 2017, *Astronomy & Astrophysics*, 602, A2
- Sopp H. M., Alexander P. 1991, *Monthly Notices of the Royal Astronomical Society*, 251, 112
- van Breugel W., Miley G., Heckman T. 1984, *Astronomical Journal*, 89, 5
- White R. L., Becker R. H., Helfand D. J., Gregg M. D. 1997, *Astrophysical Journal*, 475, 479
- Wilkinson P. N., Polatidis A. G., Readhead A. C. S., Xu W., Pearson T. J. 1994, *Astrophysical Journal Letters*, 432, L87
- Williams W. L., Intema H. T., Röttgering H. J. A. 2013, *Astronomy & Astrophysics*, 549, A55
- Williams W. L., van Weeren R. J., Röttgering H. J. A. *et al.* 2016, *Monthly Notices of the Royal Astronomical Society*, 460, 2385
- Wilman R. J., Miller L., Jarvis M. J. *et al.* 2008, *Monthly Notices of the Royal Astronomical Society*, 388, 1335